

Detection of a transiting Hot Jupiter around WASP-44

Adriana Barbieri and Alessandro Bianchetti

Dipartimento di Fisica e Astronomia "G.Galilei", Università degli Studi di Padova, Vicolo dell'Osservatorio 3, 35122 Padova, Italy

February 2022

ABSTRACT

Context. WASP-44 b is an exoplanet orbiting around its G-type parent star, located in the constellation of Cetus and discovered in 2011 by Anderson et al. 2011.

Aims. In this work, we're going to focus mainly on the transit of the exoplanet, in order to retrieve period, radius and time of transit, and we're going to search for any transit time variation signature that may be caused by the presence of a hidden perturbing companion. With this goal, we're going to study and compare two different datasets from TASTE project and TESS mission. We're going to complete the analysis with a radial velocity dataset to yield further insight on the mass and the kinematical properties of the planet. Finally, we make some considerations about the limb darkening effect through different methods (Claret et al. 2011, Claret 2017, Claret 2018).

Methods. We first examine stellar atmospheric parameters and derive stellar mass and radius by using *isochrones* (Morton 2015). We then analyse some single-night images obtained with Copernico telescope at the ground-based Asiago Astrophysical Observatory and, after proper correction, we use them to extract the light curve of the alleged planet via the TASTE project pipeline. From TESS portal we download another dataset, we select the PDCSAP (Pre-Data Conditioning Simple Aperture Photometry) lightcurve, covering multiple transit events, and we correct for systematics and detrend it. Both TASTE and TESS datasets were analysed with MCMC simulations performed by *PyORBIT*. RV dataset is taken by CORALIE spectrograph on the Euler Telescope in La Silla.

Results. We obtained for our target WASP-44 b a period $P = 2.423805 \pm 0.000021d$, a scaled radius (R_p/R_*) = $0.1170^{+0.0025}_{-0.0026}$, a mass $M_p = 0.88 \pm 0.07M_J$ and a density $\rho_p = 0.99 \pm 0.09 g/cm^3$.

Conclusions. We verified that the main planetary bulk and orbital parameters we retrieved (scaled radius, mass, density, orbital period) are consistent with the ones found in the literature and we also searched for TTV signals in the O-C diagram and in the phase-folded RV curve, finding none.

Key words. planet and satellites: detection – TESS – TASTE – CORALIE – star individual: WASP-44 – Techniques: photometric – radial velocities – planets and satellites: individual: WASP-44 b

1. Introduction

Confirmed exoplanets are growing in number year by year, and transit method is nowadays a widespread and hugely successful detection method. Most planets indeed are discovered by tracing the lightcurve and searching for any sign of a weakening in the flux. In this report we focus on WASP-44 b, a Jupiter-size planet orbiting around a G-type star, located in the constellation of Cetus. An estimate of the mass and radius of the star can be useful for the incoming planetary analysis, but first we need to borrow stellar atmospheric parameters from the literature. In a conservative spirit, we avoided any paper result which is not inferred via spectroscopy, and select Anderson et al. 2011 as our main reference for stellar parameters. This also is the discovery paper of the exoplanet under exam. In this paper, estimates of the atmospheric parameters of WASP-44 are provided via an analysis of the width of the spectral lines. As for the planet WASP-44-b, its main parameters from (ibid.) are displayed in 1.

This work develops as follows: in Section 2 we mention the theoretical frame of the transit method. In Section 3 we present atmospherical and photometric specifics of the target star WASP-44, derive stellar mass and radius and introduce the limb darkening effect, fully addressed in appendix. Section 4 is dedicated to the applied TASTE data pre-reduction pipeline and to aperture synthesis, while in Section 5 we exploit the data already reduced by TESS team, and then perform detrending and transit search.

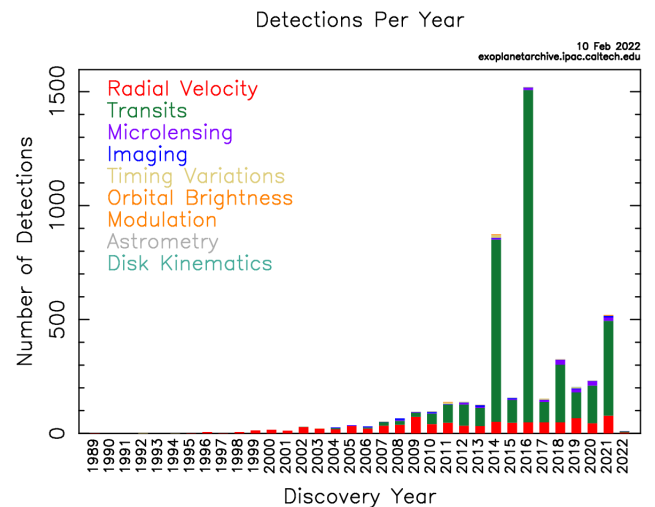


Fig. 1: Confirmed exoplanets distribution per year of detection via different methods. Credits to <https://exoplanetarchive.ipac.caltech.edu/>

Section 6 is focused on a Markov-Chain Montecarlo analysis via a dedicated routine, first for TESS, and then for TASTE with TESS priors. In section 7 we compare the estimated central time

Parameter	Value
$M(M_J)$	0.889 ± 0.062
$P(d)$	2.4238039 ± 0.0000087
$i(deg)$	$86.02^{+1.11}_{-0.86}$
(R/R_*)	0.1260 ± 0.0030
b	$0.560^{+0.076}_{-0.123}$
$K(m/s)$	138.8 ± 9.0

Table 1: Planetary parameters according to Anderson et al. 2011

of transit from the two datasets, in order to check for transit time variations (TTVs). Section 8 is dedicated to a CORALIE RV dataset analysis, aiming to complete this work with a mass estimate for the planet. In the conclusions, we sum up the main features of the planet.

2. The transit method

The transit method is a photometric indirect method of detection of exoplanets, which consists in the observation of a drop in the flux of a star due to the transit of a planet across the stellar disk. The subsequent variation of the measured stellar luminosity is proportional to the ratio of the projected areas of the planet and the star, or equivalently, the dimming of the flux is proportional to the ratio of the square of the respective radii; therefore, known the radius of the star from its spectrum, the radius of the planet can be easily obtained from the measured depth of the flux.

The modelled transit light curve is distinguished by a characteristic trapezoidal shape, whose main geometrical parameters are the impact parameter, the ingress/egress and transit duration, and the transit depth. Also, limb darkening and atmospheric effects may pollute the observational transit curve and cause a deviation from the trapezoidal model. The geometry of the system

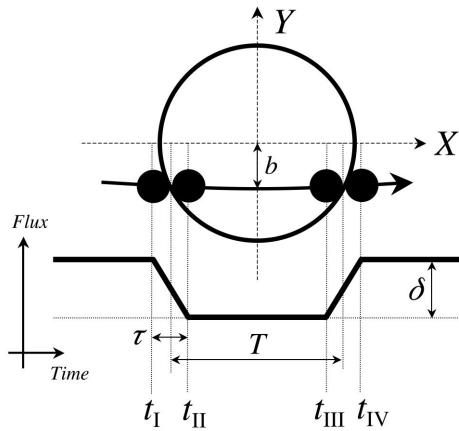


Fig. 2: Simplified transit light curve. Credits to Winn [2010]

places a strong constraint on the inclination of the orbital plane of the planet with respect to the line of sight: the transit can be observed exclusively for almost edge-on orbits, meaning orbital planes that are as parallel as possible to the line of sight. This condition yields a low probability of detection, which in turn requires a huge number of target stars to carry on successfull observations.

Furthermore, at least two transits are required to determine the orbital period of the extrasolar planet candidate, and since the duration of the transit is very short compared to the orbital

period, continuous and prolonged observations are required in order to detect it.

It is worth mentioning the selection biases that are intrinsic to this method (and to the current available technology): indeed it yields the largest detection probability for large planets orbiting very close to small and quiet stars, thus selecting Hot Jupiters around late type stars as ideal targets. Also, one has to look after false positive scenarios, meaning astrophysical phenomena mimicking transit effects, like stellar activity (spots) and stellar companion eclipses.

Transit analysis produces an estimation of planetary radius and orbital inclination: if combined with radial velocities measurements, which provides minimum mass $M_p \sin i$, this method yields planetary mass and mean density. The latter, as well as mass and radius, is important to gather information about planet formation and evolution scenarios.

3. Preliminary steps

3.1. Inferring stellar mass and radius

The H_α line was used to determine the effective temperature (T_{eff}), while the $NaI\ D$ and $MgI\ b$ lines were used as surface gravity ($\log g^*$) diagnostics (Anderson et al. 2011). The elemental abundances, including $[Fe/H]$, were determined from equivalent width measurements of several clean and unblended lines. This led to proper estimation of the atmospheric parameter triplet T_{eff} , $\log g^*$ and $[Fe/H]$. Literature errors include statistical uncertainties only. In the same conservative spirit we previously showed, we add in quadrature a further term to the errors of all three parameters (Sousa et al. 2011). This leads to the results collected in table 2 . To run the analysis routine we need also stel-

T_{eff} (K)	$\log g^*$	$[Fe/H]$
5400 ± 162	4.50 ± 0.22	0.06 ± 0.11

Table 2: Stellar atmospheric parameters from Anderson et al. 2011, with inflated errors.

lar parallax and stellar photometric information. We used Gaia eDR3 parallax $p = 2.764 \pm 0.020 \mu as$ and retrieved WISE photometric data from IRSA database¹ in 3 out of the 4 available filters (W1, W2, W3). W4 data were not available for this target. Also, photometry in the J,H and K bands were retrieved from 2MASS catalogue (Cutri et al. 2003). We then ran *isochrones*

WISE	W_1	W_2	W_3
	11.246 ± 0.022	11.301 ± 0.021	11.35 ± 0.19
2MASS	J	H	K
	11.702 ± 0.023	11.408 ± 0.025	11.341 ± 0.026

Table 3: Photometric parameters

(Morton 2015), with Bayesian approach, with posterior sampling performed by *MultiNest* . The results of the analysis are reported in table 4. Estimated stellar mass is compatible with Addison et al. 2019, as well as stellar radius. Huge errors on the age estimate are pretty common for this analysis, since stars with this mass evolve very slowly along the Main Sequence.

¹ <https://irsa.ipac.caltech.edu/Missions/wise.html>

Parameter	Value
$M(M_\odot)$	0.95 ± 0.05
$R(R_\odot)$	0.93 ± 0.01
$\rho(\rho_\odot)$	1.19 ± 0.09
$age(Gyr)$	$4.8^{+3.5}_{-2.9}$

Table 4: Stellar physical parameters derived by *isochrones*

3.2. Limb darkening correction

Limb darkening is an important effect that cannot be neglected when observing a star. In short, the edges of the luminosity profile of a star always look darker than the core: this occurs because there is a physical, constant distance L at which the optical depth is equal to unity, further than which the observations are not possible since photons are completely absorbed and do not reach the observer. This characteristic size, however, can extend deep inside the hot layers of the star if we look straight to the center, being L radial, while it only reaches the colder, outer layers if we look at the edges of the star, since L and our line of sight (LoS) are not radial anymore. Correcting for this effect

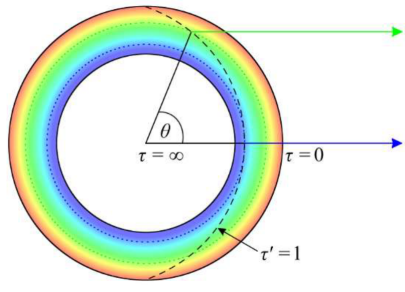


Fig. 3: Limb darkening effect scheme. Credits to <https://ediss.sub.uni-hamburg.de>

may be challenging. Indeed we can measure it directly only for the Sun, while we need to model it somehow for any other star, thus figuring out a proper law for the intensity decrease $I(\mu)$, where $\mu = \sqrt{1 - r^2}$. Many choices are plausible at this point: a uniform behaviour, a linear, a quadratic, a square-root or a logarithmic law are all valid guesses. Parametrizing such laws introduces the so-called *LD-coefficients*, which will depend on the stellar parameters. Knowing the latter relationship (for instance calibrating it based on a large sample of stars) allows to obtain the coefficients directly from the atmospheric parameters. The alternative way is to fit the light curve leaving the coefficients as free parameters. Different parametrizations for limb darkening coefficients are possible: throughout the paper, we're going to use Kipping parametrization as a reference (Kipping 2013).

The choice of the functional dependence on μ is a delicate one. Multiple modelling approaches can be followed, based on different papers. This analysis is addressed in A, where we face three different publications by the author Antonio Claret, who provided atmospheric parameters tables to calibrate a relationship between limb darkening coefficients and atmospheric parameters. The oldest paper, Claret et al. 2011, provides a variety of filters from both the Johnson system and SDSS, including filter r^* , used for TASTE analysis to minimize the atmospheric extinction and limb darkening effects. Claret 2017 and Claret 2018 are instead referred to the only TESS built-in filter and so they're available for comparison with TESS output alone.

4. TASTE data analysis

TASTE project² (Nascimbeni et al. 2011) provides ground-based observations of our target taken with Copernico 1.82m telescope at the Asiago Astrophysical Observatory, located at Mount Ekar, Asiago (VI), Italy. TASTE goal is to produce a catalog of lightcurves for selected targets using the TTV method. The imaging device is called AFOSC (Asiago Faint Object Spectrograph and Camera), with $9' \times 9'$ FoV. Data for WASP-44 were collected between $17:35:02.5'$ and $21:41:43.7'$ of 2020 November 20 (UTC), with a 15s exposure time and a r' -Sloan filter. The dataset used only contains one transit.

Before actually analysing these data, we need to properly correct them: it is of capital importance to remove instrumental effects in order to largely improve the final result. During observations, targets are defocused on purpose, to avoid saturation and minimizing the effect of pixel inhomogeneity. After proper discussion and conversion into the required format, we will prepare the configuration file for the analysis.

4.1. Bias and flat field correction

CCDs (Charged Coupled Devices) are the favourite detectors for photon counting, due to their high quantum efficiency. The images produced are raw and must be properly *pre-reduced* before being analysed. Pre-reduction goes through different steps:

- **bias** is the additive offset contribution, a zero-exposure instrumental factor. It measures the charges left on the CCD even with the shutter closed and 0 s of exposure time. The presence of these charges is related to the fact that a finite direct current is needed to move the charges from the pixels to the output register, and this introduces a bias in the science frames. It must be removed in order to isolate the photons of astrophysical origin. The other component of the bias corresponds to the so-called *readout noise*. We will remove the constant DC term and then perform an average of the bias frames to reduce RO noise, that still cannot ever be fully removed;
- a **flat field** is a calibration image obtained by illuminating homogeneously the pupil of the telescope, using twilight sky or appropriate, back-lighted screens. After correcting for bias, flat field correction factor is to be normalised and then applied on each pixel by dividing the science image counts by the estimated pixel efficiency to get to the true counts;
- **differential aperture photometry** allows us to keep track of any noise variation. By normalizing the flux of our target with that of a reference star close enough to it, any first-order systematic trend is cancelled, since any environmental or instrumental variation affects both sources. Therefore all the remaining variations are of astrophysical origin.

For pre-reductions steps, we use the *STARSKY* subroutine *HUGGY* (*ibid.*).

4.1.1. Bias correction

30 bias images with $\tau_{exp} = 0$ s are available, displaying the zero-exposure offset of the pixel board. We run *huggy.bias* to compute the average *master bias* file. We hereby plot a random bias image and the master bias to offer a concrete view of the correction. Note that the master bias frame distribution is peaked and much closer to a unique constant value, as all pixels behaved in the

² The Asiago Search for Transit timing variations of Exoplanets

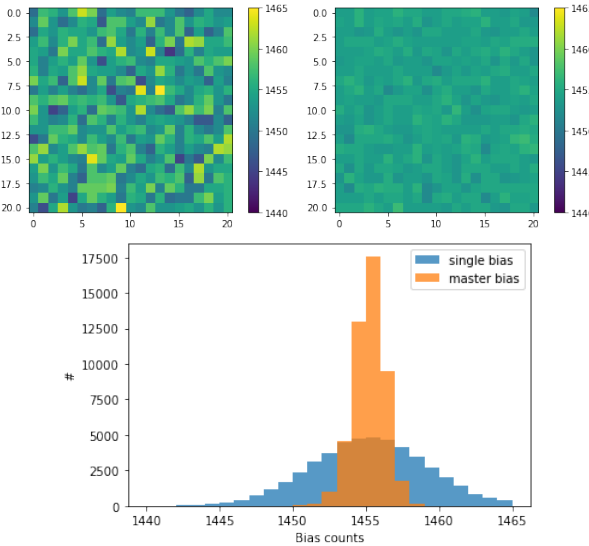


Fig. 4: Comparison between TASTE random bias frame and master bias

same way, like in an ideal situation. We can see this even numerically, by looking at the dispersions of the above distributions: $\sigma_{rb} = 3.82$ and $\sigma_{mb} = 0.89$.

4.1.2. Flat field correction

30 flat field frames with $\tau_{exp} = 2s$ are used. We run *huggy-flat.e* inputting a 90% normalization fraction, meaning the fraction of pixels we want to account for, ruling out the sides which are often polluted by overscan columns. These are visible in the form of dark stripes on the sides of any flat field taken. Then we have to input the overscan values, set to 0 as we do. Subsequently, we need to provide the master bias file, which will be subtracted from the data. Finally, we input all available flat fields. This will produce an output file showing the average response of pixels to an external light source. A normalised version of the file yields the efficiency of each pixel.

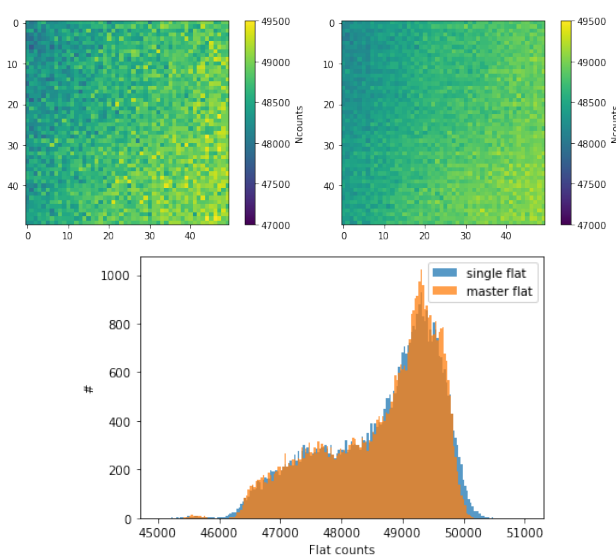


Fig. 5: Comparison between TASTE random flat field and master flat

4.2. Final correction

The final step is to apply the correction files obtained in the previous sections to science images. The final correction code requires the master bias and the normalised master flat, and of course all the 883 target images ($\tau_{exp} = 15s$). First we subtract the master bias (instrumental noise) and then we divide the pixels by the normalised master flat, thus retrieving an estimate of the actual photon counts. All this is done by running *huggy.correct.e*. The corrected images are now ready for aperture synthesis.

4.3. Extracting the light curve

We are approaching the very heart of TASTE analysis, preparing for aperture synthesis. We now need to display the science images, make sure to identify the correct target and select a proper background analysis around it. To do that, we used *ds9* to define an inner and outer radius: the former marks a circular region hosting the target, the latter defines a surrounding annulus, that is going to be the sky background reference.

The same procedure must be repeated (with the same inner and outer radii) on a properly selected reference star, close to and roughly as bright as the target.

The Equatorial J2000 coordinates from IRSA Archive³ for our host star WASP-44 and the chosen reference star are, respectively, RA = 00h 15m 36.77s, DEC = -11d 56m 17.3s and RA = 00h 15m 33.14s, DEC = -11d 54m 27.6s.

The r-Sloan photometric magnitudes for target and reference star are respectively $m = 13.021 \pm 0.005$ mag and $m = 13.058 \pm 0.005$ mag, taken from CDS Portal⁴, thus fulfilling the need of two similar stars for differential photometry.

We report instead in table 5 the coordinates from *ds9* of the target and of the chosen reference star expressed in pixel units.

	x_c	y_c
Target	170	37
Reference	288	57

Table 5: Target and reference star coordinates

$$R_{in} = 11, R_{out} = 20$$

huggy-psf.e processes the coordinates of the center of the target, the inner and outer radii, and the corrected science images, yielding information about the Point Spread Function, meaning the flux distribution as a function of the distance from the source core. The output displays the radii at which we find 68, 90, 95 and 99% of the total flux. We're not going to use the 68% aperture option in this analysis. The remaining three apertures in pixel units are $a_0 = 4.71$, $a_1 = 5.97$ and $a_2 = 8.76$ respectively. Photometry analysis is carried out by another subroutine, *sentinel.e*, which requires the coordinates of the target and of the reference stars, followed by the radii of two selected apertures from the previous output. Also, we need again inner and outer radii of the selected region for the analysis, as well as the fully corrected science images. A centroiding method is also required (we selected the Gaussian option). For a star fainter than average like ours ($J \approx 11$) the recommended choices for the apertures are 90 and 95%, in order to make sure not to run into saturation. However, all three possibilities were tested.

³ <https://irsa.ipac.caltech.edu/>

⁴ <https://cds.u-strasbg.fr/>

sentinel output is the starting point for TASTE analysis. This file contains main photometric information about target, reference star and sky flux throughout the observation session. (Fig.6). Time was converted from JD (UTC) to BJD (UTC) (B). The sky flux has been constantly decreasing in time, so we ex-

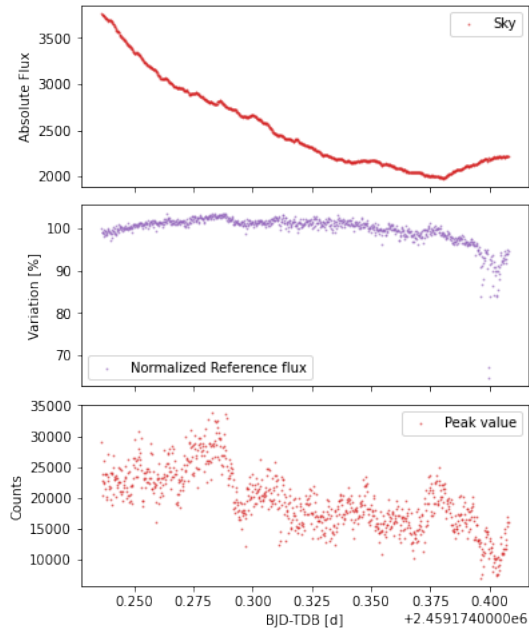


Fig. 6: Upper panel: sky background flux, every point is the median of the annulus bound by R_{in} and R_{out} . Middle panel: reference star flux, normalised to the first measurement. Bottom panel: peak points of the flux inside the defined aperture.

pect less and less disturbance as the observation proceeds. The reference star, on the other hand, seems to be pretty stable in terms of flux. We also want to make sure that reference star are correctly comoving with the target: to do that, we plot the variation in position at every time step and make sure we have similar motion (Fig.7). Plotting FWHM reveals an increasing trend, at odds with the sky pattern. Next, we compare the flux plot of all three different aperture we have chosen (Fig.8). The third case (99%) seems to be slightly less noisy: that's our first clue that this aperture might be the best suited choice for the aperture analysis. As a further goodness check, one may take a look at the peak value trend of the target source and compare it to the saturation level (Fig.9). We also plot the reference star flux to see whether they are above the quality threshold (9). We can finally visualize the transit in all three cases (Fig.10). To do that, we plot the ratio between target and reference star: *differential photometry* helps us get rid of systematic errors affecting both sources. Once again, we see that 99% aperture seems to have less dispersion than the other cases. In-transit datapoints are ruled out to perform a polynomial fit, that will be our reference trend for the stellar flux. The scatter of the fit can help us disentangle between the three apertures. To rule out transit points, we roughly select an ingress and egress time (Fig.11). A quadratic law ($p_0x^2 + p_1x + p_2$) was chosen to set things up in the most general case. A least square fitting via numpy function `np.polyfit` yields the values collected in table 6 .

We immediately notice that the linear coefficient p_1 is well compatible with zero. The offset term represents the flux continuum. We display in table 7 the standard deviation of the points of the continuous with respect to the linear fit. These quantify

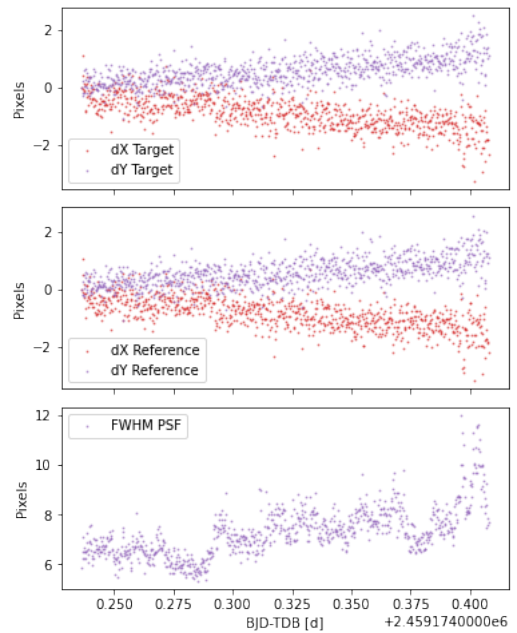


Fig. 7: Upper and middle panel: target and reference star show the same coordinate variation in the CCD. Bottom panel: full width half maximum of the peak flux.

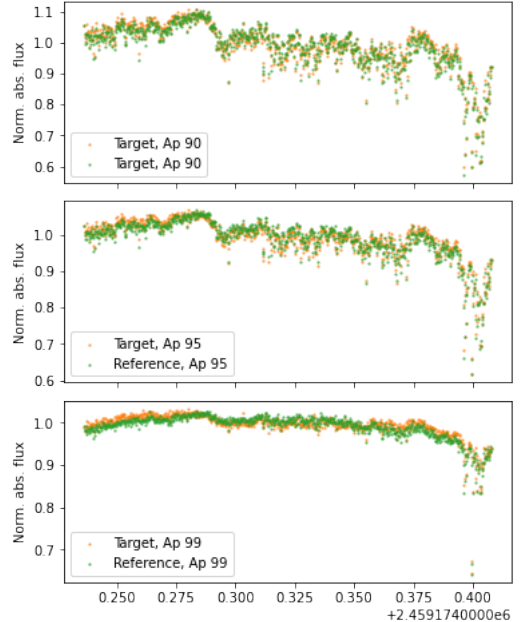


Fig. 8: From top to bottom: TASTE 90, 95 and 99% apertures, showing both the target and reference star. Dispersion is reduced as the aperture grows.

# ap	p_0	p_1	p_2
90	-0.53	0.0014	1.05
95	-0.80	0.0012	1.06
99	-0.91	0.0014	1.06

Table 6: TASTE polynomial fit parameters

scattering and indicate that the 99% aperture is indeed the best photometric choice, having the smallest standard deviation.

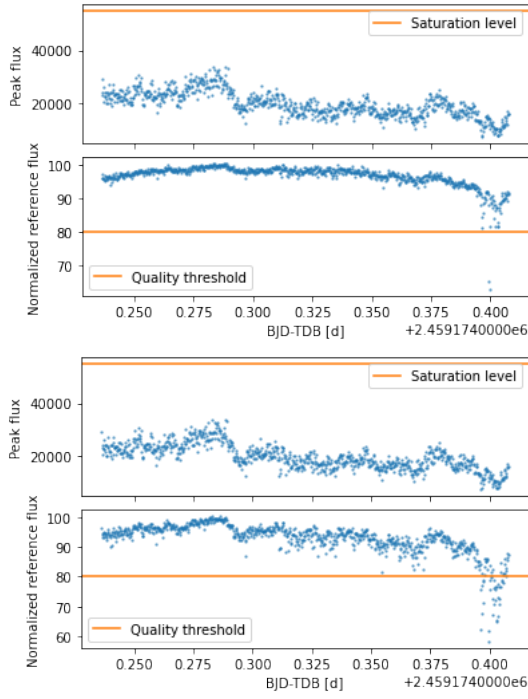


Fig. 9: TASTE apertures. Upper panel: widest aperture, bottom panel: narrowest aperture. In both cases the peak value is well below the saturation limit, and we also see that the reference data are above the required threshold. A few points at late times are below the quality factor in the 90-95% case, thus supporting the choice of the widest aperture at 99%.

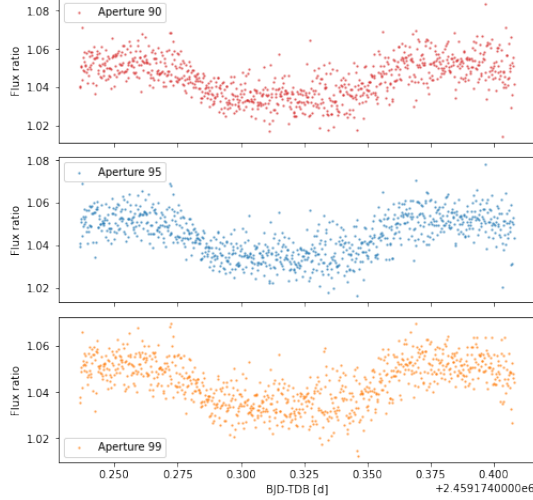


Fig. 10: TASTE transit image for growing aperture, top to bottom. Note that the above case (90%) shows the most outliers.

σ_{90}	0.0063
σ_{95}	0.0061
σ_{99}	0.0059

Table 7: Standard deviation of TASTE polynomial fit for three the selected photometric apertures

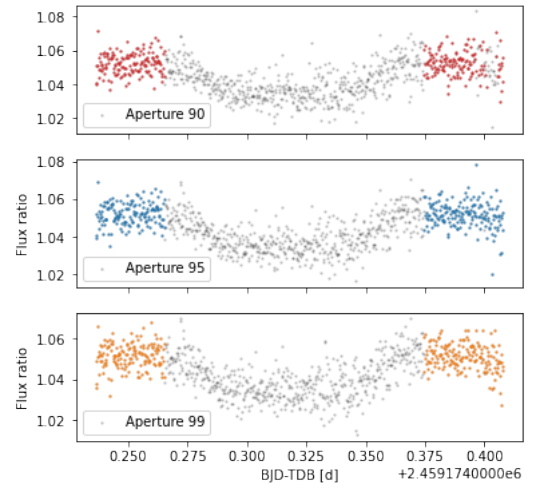


Fig. 11: Time boundaries for the TASTE transit are roughly ballparked to prepare a proper, flat dataset to fit with a second degree polynomial.

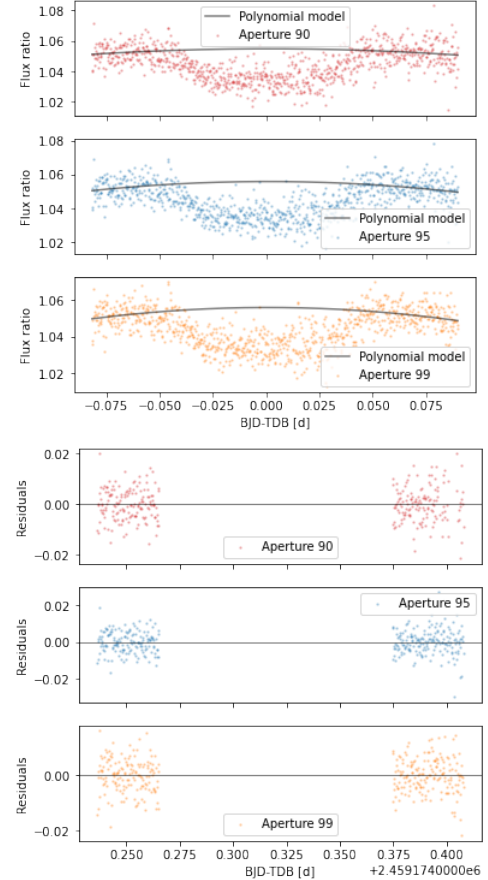


Fig. 12: Polynomial fit on TASTE flux and residuals for the three aperture cases. Before doing the fit, data were shifted so that the central time was placed approximately to zero.

5. TESS data analysis

TESS (Transiting Exoplanet Survey Satellite) space mission was launched on April 18, 2018, aboard SpaceX Falcon 9. Its main goal is to search for transiting planets orbiting relatively bright stars ($V < 11$). During its 2-years nominal mission, TESS ob-

served 26 different sectors, each $24^\circ \times 96^\circ$ wide and observed for a time span of 27 days. Full sky images are provided with a cadence of 30 minutes, while target pixel files (TPF) are obtained pointing at pre-selected targets, observed with a cadence of 2 minutes. WASP-44 was observed by TESS in 120s-cadence mode during observations of sector 3, between 2018 September 20 and October 17. The photometric observations for WASP-44 were reduced by the Science Processing Operations Center (SPOC) pipeline (Jenkins et al. 2016): all results are available on the MAST platform (Mikulski Archive for Space Telescopes)⁵. From ExoFOP-TESS⁶ we retrieved the TIC (TESS Input Catalog) identification number for our target star (12862099). We were then able to access MAST and download the TESS 2-min cadence TPF, which is a 11x11 pixels cutout centered in the target, produced via the *Lightkurve*⁷ package for Kepler and TESS. We performed a preliminary contamination check with *tpfplotter*⁸, aiming to establish whether our default photometric aperture includes any contaminant star that may cause a dilution of the transit. By running *tpfplotter* we obtained Fig.13, which shows how only one star is present within the aperture, but since it is over 4 magnitudes fainter than the target in the G band, it does not constitutes a contaminant and can therefore be ignored. We use the mask provided by TESS science team (Fig.14).

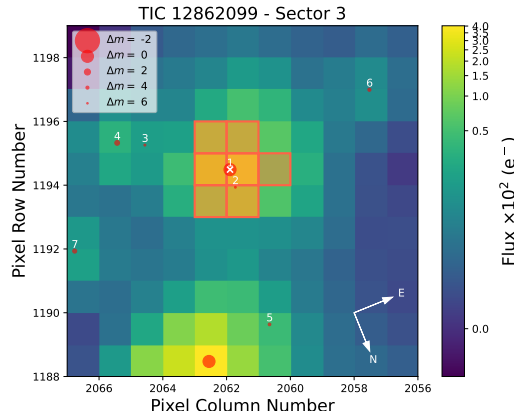


Fig. 13: TPF plot. The featuring contaminant is faint enough to be neglected.

5.1. Light curve extraction via aperture photometry

SPOC pipeline yields two lightcurves: SAP (Simple Aperture Photometry), which is corrected for background only, and PDC-SAP (Pre-search Data Conditioning Simple Aperture Photometry) which is corrected for any systematics.

We proceeded to perform aperture and time series photometry on the TPF in order to select only the pixels belonging to the optimal aperture; from the obtained calibrated pixels, we derived the transit and the background flux light curves.

Afterwards, we removed from the time series dataset of the optimal aperture all the TESS cadences flagged as anomalous ($\text{flag} > 0$) or encoded as NaN. The list of bits that were checked for anomalies is reported in table 8 and further information on

⁵ <https://mast.stsci.edu/portal/Mashup/Clients/Mast/Portal.html>

⁶ Exoplanet Follow-up Observing Program for TESS website, to be found at <https://exofop.ipac.caltech.edu/tess/>

⁷ <https://github.com/lightkurve/lightkurve>

⁸ <https://github.com/jlillo/tpfplotter.git>

Masked WASP-44 Cal. Fluxes - Sector 3, Second Cadence

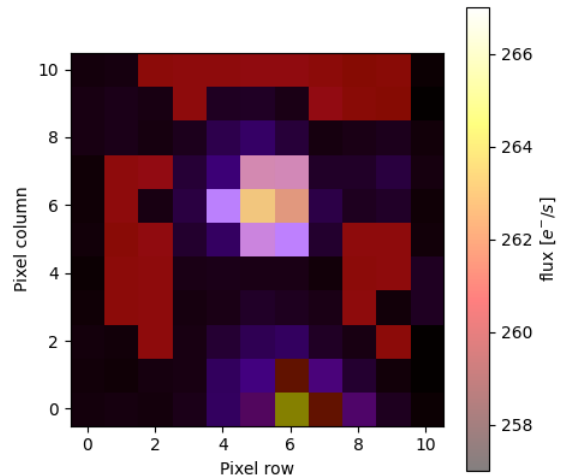


Fig. 14: Masked TPF

flagged data can be found in TESS Science Data Product Description Document⁹. The result of this quality selection can

Bit	Value	Description
1	1	Attitude Tweak
2	2	Safe Mode
3	4	Spacecraft is in Coarse Point
4	8	Spacecraft is in Earth Point
5	16	Argabrightening event
6	32	Reaction Wheel desaturation Event
8	128	Manual Exclude. The cadence was excluded because of an anomaly
10	512	Impulsive outlier removed before cotrending
12	2048	Straylight from Earth or Moon in camera FOV (predicted)
13	4096	Scattered Light Exclude (sopc-4.0.5 and later)

Table 8: Data quality flags

be seen in Fig.15. Subsequently we repeated the quality selection analysis on the lightcurve files (provided by the TESS team and obtained from the MAST portal as previously addressed), and plotted both the optimal aperture, the SAP and the PDC-SAP fluxes thus obtained as a function of time (Fig.16). The observed overlapping between the optimal aperture and the SAP lightcurve is evidence for the goodness of the lightcurve extraction we performed. For our photometric analysis, however, we will make use of the PDCSAP light curve, being it usually cleaner than the SAP flux and also corrected for systematic trends.

5.2. Detrending methods

It is of capital importance to flatten and de-trend the PDCSAP lightcurve, meaning to correct for stellar activity, flares, gaps in the data and interrupted transits by removal of the curve modulation due to the stellar and instrumental systematics. Via the *WOTAN* package¹⁰ (Hippke et al. 2019a) we applied to the PDCSAP light curve a biweight filter with a time window of 1 d and a hspline filter with a time window of 2 d (17); afterwards we normalized and folded the lightcurves, with the aim of studying the transits in phase (18). We obtained for the PDCSAP,

⁹ <https://heasarc.gsfc.nasa.gov/docs/tess/documentation.html>

¹⁰ <https://github.com/hippke/wotan>

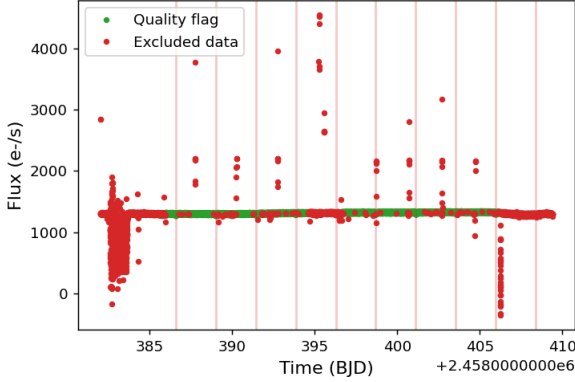


Fig. 15: Flux derived from the calibrated pixels (up) and detail of the first cadence (bottom).

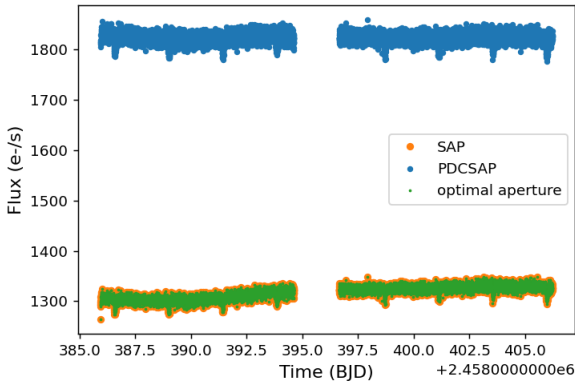


Fig. 16: Optimal aperture, SAP and PDCSAP lightcurves.

biweight and hspline fluxes' standard deviations the values of 0.00441, 0.00406 and 0.00408 respectively. Therefore, having the smallest σ , we considered the flattened biweight lightcurve as the most accurate one.

5.3. Identification of periodic signals

We proceeded to perform an iterative transit search on the detrended light curve in order to independently confirm the detection of the periodic signals in the TESS light curve. We used the Transit Least Squares (TLS)¹¹ algorithm (Hippke et al. 2019b),

¹¹ <https://github.com/hippke/tls>

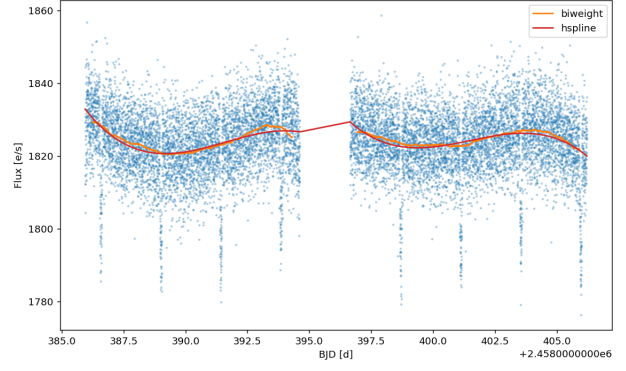


Fig. 17: Hspline and biweight filters.

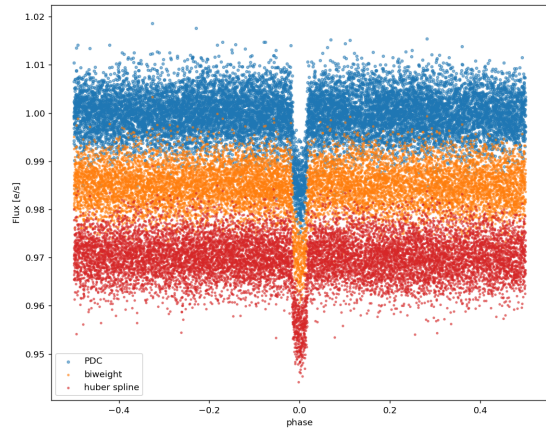


Fig. 18: Flattened and folded data. With respect to 17 the difference in flux can be now appreciated

which offers one of the best methods to detect planetary transits from time-series photometry. Indeed it searches for transit-like features with stellar limb-darkening, includes the effects of planetary ingress and egress, analyses the entire data of the phase-folded light curve and yields a 10% higher signal detection efficiency (SDE) compared to the Box-fitting Least Square (BLS) method, therefore being more accurate but more time-consuming.

Proof of this is the periodogram (19) and folded lightcurve (20) with a satisfactory SDE of 15.15, a preliminary period $P_{TLS} = 2.425d$, central transit time $T_{c,TLS} = 2458386.573d_{BJD}$ and a best transit duration of $\tau = 0.072d$ (roughly 1h43min). At last, we chose to select only the data points that are at a distance which is within twice the value of the transit duration from the center of the transit. This is just a technicality to save time in the next part of the analysis (PyORBIT run). We saved the output in a data file that will be the basis for the subsequent analysis and we plotted the resulting transit light curve in Fig.21.

6. Light curve fit

Once obtained the dataset and prepared the .yaml configuration file for TESS analysis, we fitted the transit light curve with a planetary model. Afterwards we proceeded to repeat the whole

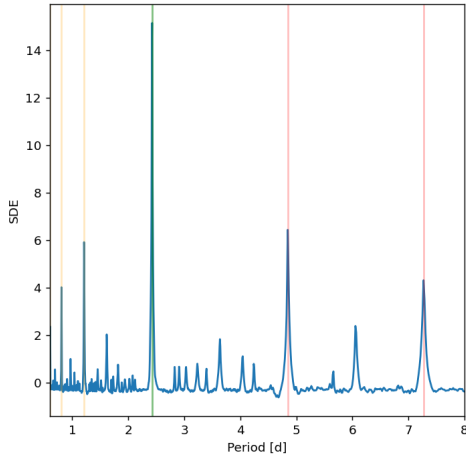


Fig. 19: TLS periodogram is very clean, ensuring effective transit detection.

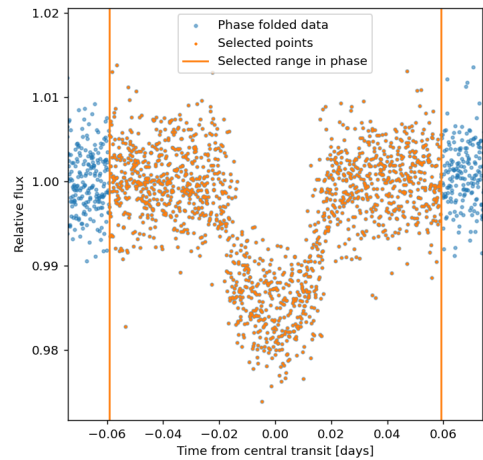


Fig. 21: Final selection

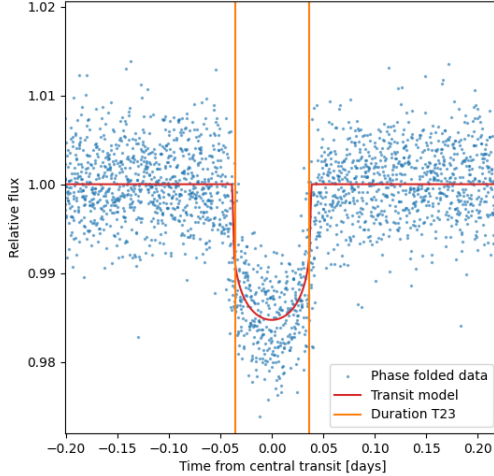


Fig. 20: Detrended transits

procedure for TASTE using the TESS results as priors. We performed both analysis using *PyORBIT*¹² (Malavolta et al. 2016, Malavolta et al. 2018), a framework for the characterization of planetary systems that is able to analyse photometry, RVs and ancillary data and to model stellar activity and transit time variations.

All the planetary transits were modelled using the Python package *BATMAN* (Kreidberg 2015); we used also the differential evolution tool *PyDE*¹³ to perform global optimization of the input parameters in combination with the affine-invariant Markov chain Monte Carlo (MCMC) sampler *EMCEE* (Foreman-Mackey 2013), which took the results of *BATMAN* as starting points for the chains. Autocorrelation analysis of the chains is also performed. Both for TASTE and TESS, we ran a total of 100000 chain steps, from which we cut 20000 steps as burn-in transient phase. In the configuration files of both analy-

ses the orbits were assumed to be tidally circularized, meaning $e = 0$, conventionally associated to a an argument of the pericenter $\omega = \pi/2$. A jitter flag was activated in order to add a jitter parameter in quadrature to the flux errors to compensate for their under-estimation. Finally, we model the limb darkening coefficients with a quadratic law, using Kipping parametrization (Kipping 2013).

6.1. TESS Data Analysis

For the Bayesian analysis of the TESS lightcurve, we assumed a circular orbit, and uniform priors for the period and the central time of transit. P and T_c were given symmetric intervals centered in the TLS estimates, in order to define boundaries for the MCMC analysis: we picked $\delta_P = 0.1 \cdot P_{TLS}$ and $\delta_{T_c} = 1/27$ as semi-intervals. Uniform priors were also assigned to the impact parameter and the scaled planetary radius. Gaussian priors based on the literature were instead settled for the stellar parameters (mass, radius, density). Limb darkening coefficients are left to vary freely. Since the resulting chains were more than 50 times longer than the autocorrelation function, we are assured that the estimate can be trusted. The physical and derived parameters obtained from the posterior samples are collected in table 9. It should be noticed that the planetary parameters are compatible with literature. In particular TESS period $P = 2.42385 \pm 0.00017$ is compatible with $P = 2.423802^{+0.000032}_{-0.000030} d$ (Addison et al. 2019) and $P = 2.4238120 \pm -0.0000012 d$ (Turner et al. 2016) within 1σ . As for the scaled planetary radius, TESS estimates yields $(R_p/R_*) = 0.1170^{+0.0025}_{-0.0026}$, compatible with Harris V filter observation $(R_p/R_*) = 0.1164 \pm 0.0017$ by ibid. Finally, orbital inclination i is compatible with $i = 85.98^{+0.39}_{-0.35}$ by Addison et al. 2019. The corner plots of the posterior samples showing the correlation between the parameters are reported in C.1. The normalized stellar fluxes, fitted with the model of the exoplanetary transit, along with the residuals are reported in Fig.22. Concerning limb darkening coefficients, we can compare these outputs to the models introduced by Claret. Claret 2017 and Claret 2018 present LD models related to TESS filter. In the above analysis, no prior was used for LD coefficients estimates, making them independent on Claret models. The comparison between such estimates (table 9) and both Claret 2017 and Claret 2018 (see A) shows pretty

¹² <https://github.com/LucaMalavolta/PyORBIT>

¹³ <https://github.com/hpparvi/PyDE>

Physical	Value
$P(d_{BJD})$	2.42385 ± 0.00017
$T_c(d_{BJD})$	$2458386.57819^{+0.00073}_{-0.00070}$
b	$0.526^{+0.047}_{-0.052}$
R_p/R_\star	$0.1170^{+0.0025}_{-0.0026}$
$\rho(\rho_\odot)$	$1.211^{+0.089}_{-0.088}$
$c1_{ld}$	$0.51^{+0.26}_{-0.28}$
$c2_{ld}$	$0.17^{+0.40}_{-0.39}$
σ_{jlt}	$0.00024^{+0.00022}_{-0.00014}$

Derived	Value
$i(^{\circ})$	$86.27^{+0.43}_{-0.42}$
R_p/R_J	1.057 ± 0.027

Table 9: Physical and derived parameters obtained from TESS analysis

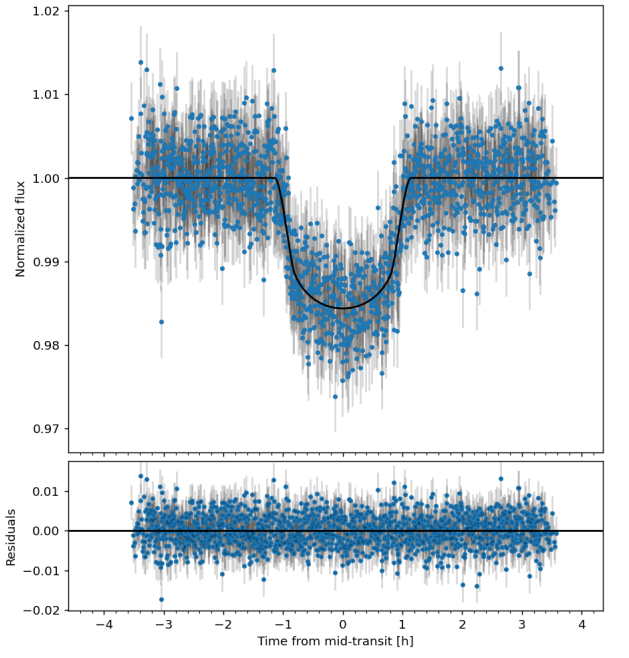


Fig. 22: TESS lightcurve

Physical	Value
$P(d_{BJD})$	2.42385 ± 0.00017
$T_c(d_{BJD})$	$2459174.31781 \pm 0.00057$
b	$0.553^{+0.038}_{-0.042}$
R_p/R_\star	0.1283 ± 0.0035
$\rho(\rho_\odot)$	$1.168^{+0.091}_{-0.089}$
$c1_{ld}$	0.51 ± 0.013
$c2_{ld}$	0.1699 ± 0.0060
σ_{jlt}	$0.00031^{+0.00034}_{-0.00036}$
p_{c0}	1.0538 ± 0.0010
p_{c1}	-0.0019 ± 0.0050
p_{c2}	$-0.58^{+0.21}_{-0.22}$

Derived	Value
$i(^{\circ})$	$86.03^{+0.38}_{-0.37}$
R_p/R_J	$1.160^{+0.036}_{-0.035}$

Table 10: Physical and derived parameters obtained from TASTE analysis

Check C.1 for corner plots and Fig.23 for the fitted transit.

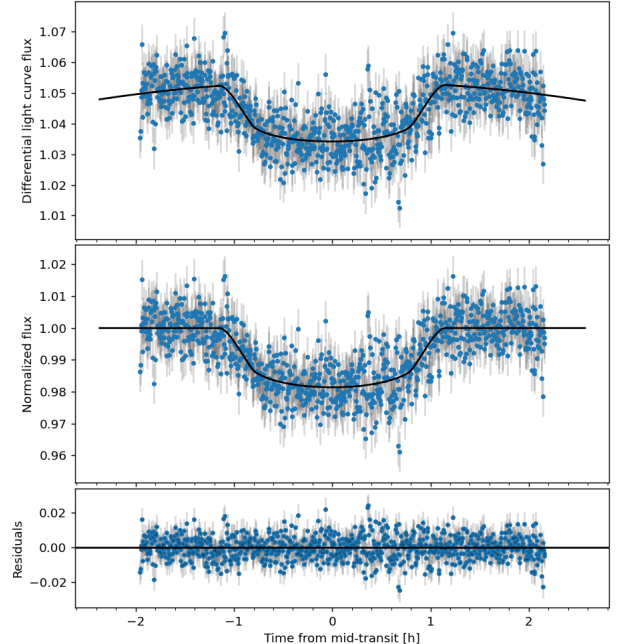


Fig. 23: TASTE lightcurve. Residuals are double those of TESS.

different results. However, TESS estimates have errorbars large enough to make such results compatible.

6.2. TASTE Data Analysis

As for TASTE lightcurve, we chose a second order polynomial trend as a model for out of transit flattening, TESS priors for the period, Claret et al. 2011 priors for the limb darkening coefficients, gaussian priors for the stellar parameters and uniform priors for all the other parameters. Since the resulting chains were more than 50 times longer than the autocorrelation function, we are again confident that the estimate can be trusted.

The physical and derived parameters obtained from the posterior samples are collected in table 10. As expected, the period is perfectly compatible with the TESS fit value.

In the configuration file for TASTE, LD quadratic coefficients priors taken from (ibid.) were inputted, so TASTE results for c_1 and c_2 are anchored to that input. Regarding photometry in the same filter (r' from SDSS), Addison et al. 2019 reports LD coefficients which are largely compatible with Claret 2011 results (see A).

7. Search for TTV signals

The transit time variation (TTV) is a sensitive method for the detection of additional planets in compact planetary systems; indeed, in the case of single-planet systems, the transit in front of the host star is expected at very regular time intervals, hence producing periodic keplerian signals. Whereas a further unknown

planet is present, it will gravitationally perturb the observed transiting planet causing a deviation from its constant periodicity and a departure of the mid transit time from the expected linear keplerian ephemeris. The amplitude of the TTV signal is proportional to the mass of the perturber and is enhanced in case of low-order (mean motion) orbital resonances between the unknown planet and the transiting one.

We apply the O-C method in order to compare the observed (O) central transit time (from TASTE observations) to the expected calculated (C) value (TESS results) and to search for any TTV signature. Linear ephemeris test shows that TASTE has a variation with respect to the TESS value T_c propagated in time. The simple calculation

$$T_c^{calc} = T_c^{TESS} + P \cdot E, \quad E = \text{int}\left(\frac{T_c^{TASTE} - T_c^{TESS}}{P}\right)$$

yields $E \approx 525$ (number of cycles) and a variation O-C= $-0.011308d$ between observed TASTE value and predicted one, that correspond roughly to 16.28 minutes.

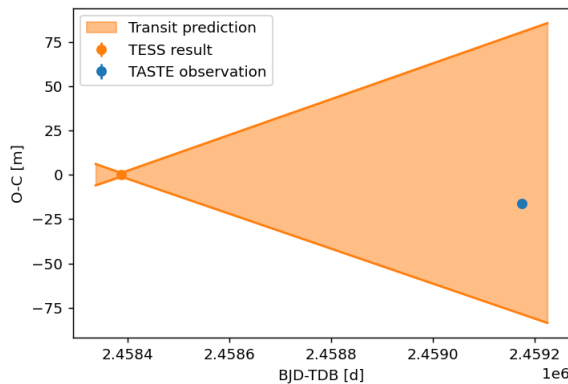


Fig. 24: O-C plot: checking compatibility between TESS prediction and TASTE result.

The observed-calculated diagram (Fig.24) shows the propagation of the error on TESS prediction, increasing throughout time up to the epoch of TASTE measurement. See that TASTE result falls within the cone, proving compatibility of the two results. The O-C variation is compatible with the mentioned number of cycles, since errors on T_c propagate through each cycle, so we don't associate such variation to a TTV signal. Therefore from this analysis there seems to be no evidence hinting at the presence of further planets in the planetary system.

8. Radial velocity analysis

Knowing the RV semi-amplitude K_* and the mass M_* of the star, the planetary mass M_p is obtained by inverting the following equation.

$$K_* = \frac{1}{\sqrt{1-e^2}} \frac{M_p \sin i}{(M_* + M_p)^{2/3}} \left(\frac{P}{2\pi G}\right)^{-1/3} \quad (1)$$

where $M_p \sin i$ represents a *minimum mass estimate*. i can be measured for a transiting planet, thus yielding M_p . Between July the 1st, 2010 at 08:28 UTC and October the 13th, 2010 at 03:50 UTC the CORALIE spectrograph mounted on the 1.2-m Euler-Swiss telescope in La Silla Observatory was pointed at WASP-44 (Anderson et al. 2011). CORALIE is used in conjunction with

the Leonhard Euler Telescope to conduct high precision radial velocity measurements, to search for exoplanets in the southern hemisphere. CORALIE is capable of measuring the motion of a star with a precision of about 11km/h (3m/s). It is housed in an isolated and stable environment with regulated temperature to guarantee long-term stability of the measurements. Its design was inspirational for later instruments, as HARPS, which is much more sensible. For WASP-44, 17 optical spectra were obtained, yielding a RV time series. We made sure the time range of this set did not overlap with the time range of the transits, since that interval is subject to Rossiter-McLaughlin effect.

We ran PyORBIT again to fit the RV curve with a 1-planet model, using N=100000 steps with a burn-in cut of 25000. Inclination was fixed to the value obtained by TESS analysis and Gaussian priors obtained from TESS best-fit values were set on P and T_c . Radial velocity input data file can be equipped with an extra "0" column (in addition to the one already present accounting for the jitter term), in order to enable the code to compute any RV offset due to the peculiar velocity of the star. Two models were exploited for the analysis: *radial velocities* and *harmonics*.

We are reasonably impelled to fit two different models since RV signals include planetary signals, but also stellar signals. Short-term stellar activity represent a polluting agent, since it is induced by spots, rotating with the stellar surface. Given that several active regions rotating with the star are present simultaneously on the stellar surface, the observed RV signal induced by short-term activity is characterized by signals at the stellar rotation period P , and its harmonics ($P/2, P/3\dots$). Whenever a signal in the RVs shows a periodicity comparable to P or its harmonics, it is very likely induced by active regions.

Results from the two models are collected in tables 11 and 12. This observation signals that the mother star WASP-44 is pretty inactive, as also shown from CaII observations (Turner et al. 2016).

The simplest model (*radial velocities*) is chosen rather than *harmonics* because of an unaltered PyORBIT run and slightly smaller errorbars. The results include an improved result for period $P = 2.42381 \pm 0.00002d$ and a central transit time $T_c = 2458386.5782 \pm 0.0007d$, consistent with TESS prior. Moreover, we obtain a radial velocity amplitude $K = 137.52_{-10.09}^{+10.55} m/s$ which is fully compatible with the literature value $K = 136.5_{-9.6}^{+10.0} m/s$ (Addison et al. 2019). Same for $M_p/M_J = 0.88 \pm 0.07$, to be compared with $M_p/M_J = 0.860_{-0.068}^{+0.072}$ (ibid.) and $M_p/M_J = 0.867 \pm 0.064$ (Turner et al. 2016). The huge errorbars found on the jitter term make it far from significative: nothing shows evidence of orbital external perturbation by any gravitational source. The RV offset $v_{off} = -4043.8_{-6.8}^{+7.0} m/s$ is also compatible with $-4045.1_{-6.2}^{+7.0} m/s$ (Addison et al. 2019).

We can also derive the planetary bulk density, BY combining the mass estimate we have just obtained with the radius estimate from TESS (9): that yields $\rho_p = 0.75 \pm 0.06 \rho_J$. We can take the reference value for Jupiter density ¹⁴ to be $\rho_J = 1.3262 \pm 0.0003$. Therefore $\rho_p = 0.99 \pm 0.09 g/cm^3$, which is compatible with $\rho_p = 0.81_{-0.16}^{+0.19} g/cm^3$ (ibid.) and $\rho_p = 1.14 \pm 0.15 g/cm^3$ (Turner et al. 2016) within one errorbar.

The phase-folded RV curves obtained from the fitting with both models are reported in 25 and 27 and the correlation plots are collected in C.2.

¹⁴ <https://ssd.jpl.nasa.gov/planets>

Physical	Value
$\sigma_{ jit}$	$8.38^{+8.85}_{-5.76}$
$v_{ off}(m/s)$	$-4043.80^{+7.00}_{-6.80}$
$P(d_{BJD})$	2.423805 ± 0.000021
$T_c(d_{BJD})$	2458386.5781 ± 0.0007
$K(m/s)$	138^{+11}_{-10}

Derived	Value
$M(M_J)$	0.88 ± 0.07
$i(deg)$	$86.28^{+0.43}_{-0.44}$

Table 11: Physical and derived parameters obtained from *radial velocities* model.

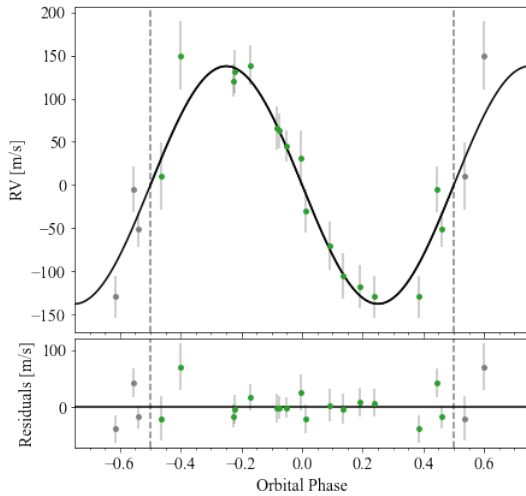


Fig. 25: Phase-folded curve from the *radial velocities* model. No systematic effect is detected on the residuals, indicating that the model is correctly followed by data, thus proving that the assumption of zero eccentricity and only one planet in the model is compatible with the observations.

We also tested the hypothesis that the RV variations are due to spectral-line distortions caused by a blended eclipsing binary or star spots and changes in the stellar atmosphere, by performing a line-bisector analysis (Queloz, D. et al. 2001). Line bisectors are defined as the loci of the midpoints on the horizontal lines extending from one side to the other of spectral line profiles. The lack of correlation between bisector span (measurement of the inverse of the mean slope of the bisector) and RV (Fig.26) rules out the null hypothesis and supports another conclusion: the periodic dimming of the flux and the RV variation of the system are due to the reflex motion of the star caused by the presence of the transiting planet.

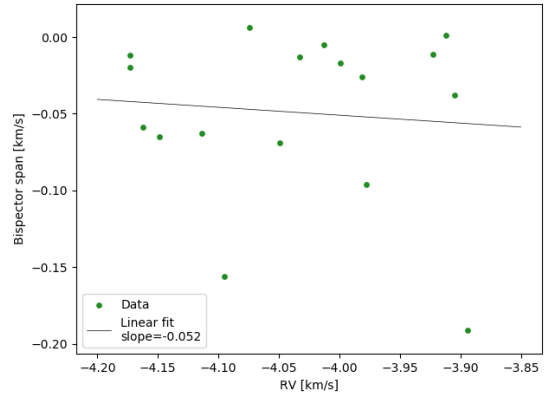


Fig. 26: RV data vs line bisector span.

In the case of the *harmonics* model, a warning by PyORBIT stated that MC chains were too short. This probably means that we did not achieve a stationary distribution in the MCMC algorithm, therefore the estimates and the autocorrelation function should be treated carefully.

Physical	Value
$\sigma_{ jit}$	$8.57^{+9.20}_{-5.79}$
$v_{ off}(m/s)$	$-4043.89^{+7.22}_{-7.05}$
$P(d_{BJD})$	$2.42^{+0.000030}_{-0.000028}$
$T_c(d_{BJD})$	$2458386.5780^{+0.00071}_{-0.00071}$
$K(m/s)$	$136.20^{+12.97}_{-15.24}$

Derived	Value
$M(M_J)$	$0.87^{+0.09}_{-0.11}$
$i(deg)$	$86.27^{+0.43}_{-0.42}$

Table 12: Physical and derived parameters obtained from *harmonics* model.

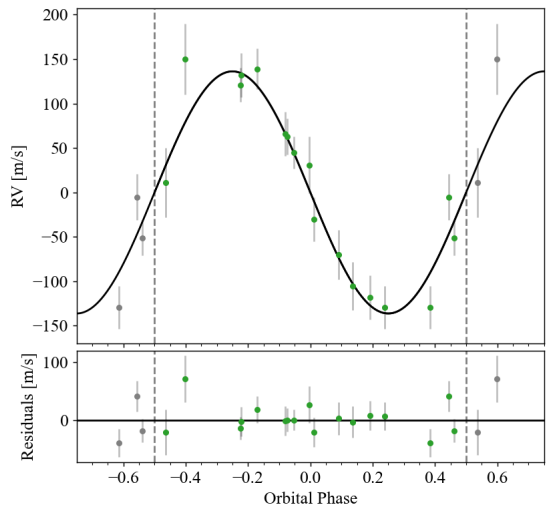


Fig. 27: Phase-folded radial velocity curve from the *harmonics* model.

9. Conclusions

The main goals of this work were to extract the lightcurve both from ground-based TASTE observations and TESS space data,

to compute mid-transit time of TESS (reliable because obtained from several transits) and TASTE and to check whether the latter falls inside the propagated prediction of the former, with the aim of searching for a TTV signal between the prediction of the linear ephemeris and the observations in the reported O-C diagram. No significant evidence for a possible transit time variation was detected.

A comparison with the literature is also due: compatibility was found for the period and for the scaled planetary radius estimated from TESS data.

In addition to the photometric analysis, RV data from CORALIE were exploited to enable a mass estimate. Reasonable agreement with the literature were obtained for the planetary mass, the bulk density and the radial velocity amplitude; furthermore the phase-folded RV curve residuals showed no significant systematic trends.

WASP-44 b is a planet with mass $M_p = 0.88 \pm 0.07 M_J$, radius $R_p = 1.057 \pm 0.027 R_J$, bulk density $\rho_p = 0.99 \pm 0.09 g/cm^3$ and orbits with a period of $P = 2.423805 \pm 0.000021 d$ around a pretty inactive parent star. In conclusion, no evidence of orbital perturbation due to an extra planetary body was found.

References

- Anderson, D.R. et al. (2011). In: *MNRAS* **422**.
- Claret, A. et al. (2011). In: *A&A* **529**, A75.
- Claret, A. (2017). In: *A&A* **600**, A30.
- Claret, A. (2018). In: *A&A* **618**, A20.
- Morton, T.D. (2015). In: eprint: 1503.010.
- Sousa, S.G. et al. (2011). In: *A&A* **533**, A141.
- Cutri, R. M. et al. (2003). In:
- Addison, Brett et al. (2019). In: *PASP* **131**, p. 115003.
- Kipping, David M. (2013). In: *MNRAS* **435**, pp. 2152–2160.
- Nascimbeni, V. et al. (2011). In: *AAP* **527**, A85.
- Jenkins, J.M. et al. (2016). In: *SCA IV* **9913**.
- Hippke, M. et al. (2019a). In: *Astrophysics Journal* **158**, p. 143.
- Hippke, M. et al. (2019b). In: *A&A* **623**, A39.
- Malavolta, L. et al. (2016). In: *A&A* **588**, A118.
- Malavolta, L. et al. (2018). In: *AJ* **155**, p. 107.
- Kreidberg, L. (2015). In: *PASP* **127**, p. 1161.
- Foreman-Mackey (2013). In: *PASP* **125**, pp. 306–312.
- Turner, Jake D. et al. (2016). In: *MNRAS* **459**, pp. 789–819.
- Queloz, D. et al. (2001). In: *A&A* **379**, pp. 279–287.
- Stassun, Keivan G. et al. (2019). In: *AJ* **158**, p. 138.
- Collaboration, Gaia (2018). In: *AAP* **616**, A1.
- Bonomo, A. et al. (2017). In: *A&A* **602**.

Appendix A: Limb darkening analysis

Appendix A.1: Claret 2017

We can represent data tables in Claret 2017 as 2D histograms, after proper unfolding of the data tables attached to the paper. To do that, we first fix metallicity, then gravity and see how the corresponding LD coefficients c_1 and c_2 depend on all three atmospheric parameters. We immediately visualize a vertical gradient rather than a horizontal one, showing that temperature dependence is very

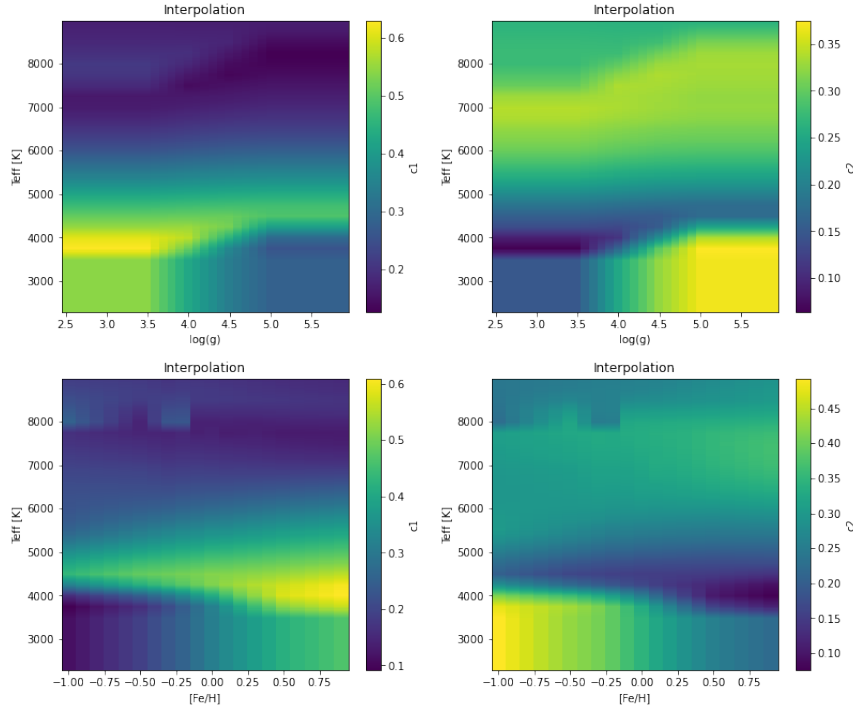


Fig. A.1: LD coefficient with fixed metallicity (top panels), fixed gravity (bottom panels)

strong. Turns out LD coefficients are essentially a function of temperature, and minor dependences on gravity and metallicity can be barely appreciated. A relevant dependance on gravity and metallicity can only be noticed at high temperatures, where we should

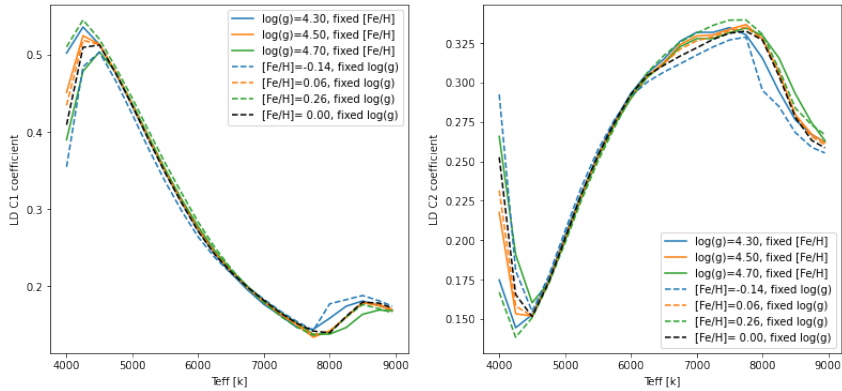


Fig. A.2: LD coefficient as a function of atmospheric parameters. Curves deviate at $T \leq 4500K$ and $T \geq 8000K$. Central part of the function is not sensitive to gravity and metallicity, both for c_1 and c_2 .

carefully select the proper curve. However, in the range we're interested in ($\approx 5400K$) the curve is degenerate and the choice of these parameters is secondary.

We perform a Montecarlo simulation, generating 1000 random atmospheric parameters around the actual ones, using the reference errorbar, thus conserving the error scale. This expedient will enable us to consider the result of this analysis as a good physical estimate of the LD coefficients. Even in this case we see that the distribution of the fixed-metallicity estimates is almost overlapping with the fixed-gravity one, thus confirming that, according to the exploited table, c_1 and c_2 not very sensitive on metallicity and gravity. For both coefficients, the two estimates coming from metallicity and gravity fixing are well compatible, thus authorizing a weighted average: $c_1 = 0.366 \pm 0.019$ and $c_2 = 0.243 \pm 0.011$.

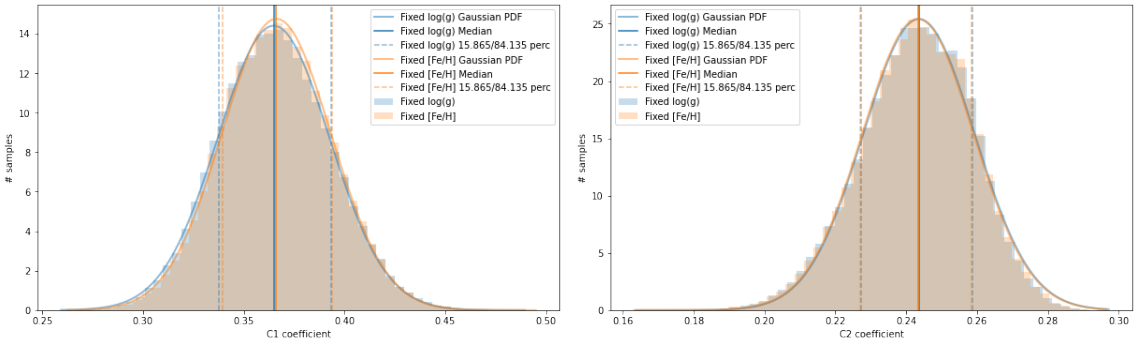


Fig. A.3: Montecarlo simulation for c_1 (left) and c_2 (right), for fixed metallicity and for fixed gravity.

	c_1	σ_{c1}	c_2	σ_{c2}
Fixed $[Fe/H]$ Median	0.3662	0.0271	0.2433	0.0157
Fixed $\log g$ Median:	0.3648	0.0277	0.2436	0.0157

Another way to deal with the same table is by selecting from the set two values of metallicity or gravity, an upper and lower limit, instead of just one reference value. This way we build two matrices and interpolate between the two to get to the desired result. The rest of the procedure is identical, leading to similar estimates of the LD coefficients. Degeneracy is less pronounced if

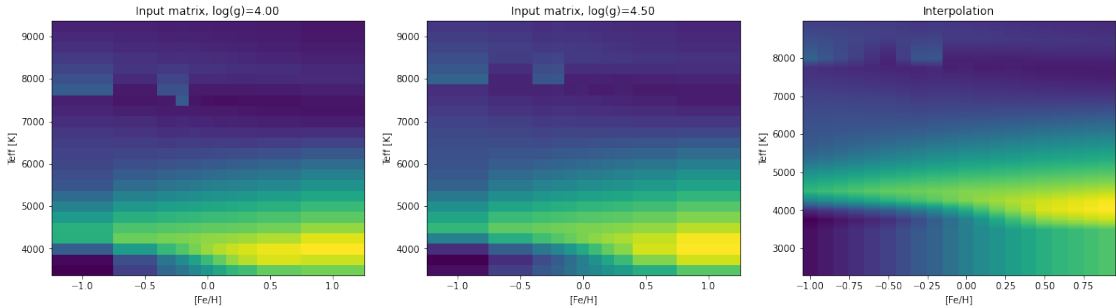


Fig. A.4: Matrices obtained by fixing gravity to $\log g = 4.0$ and to 4.5 , plus the interpolated matrix

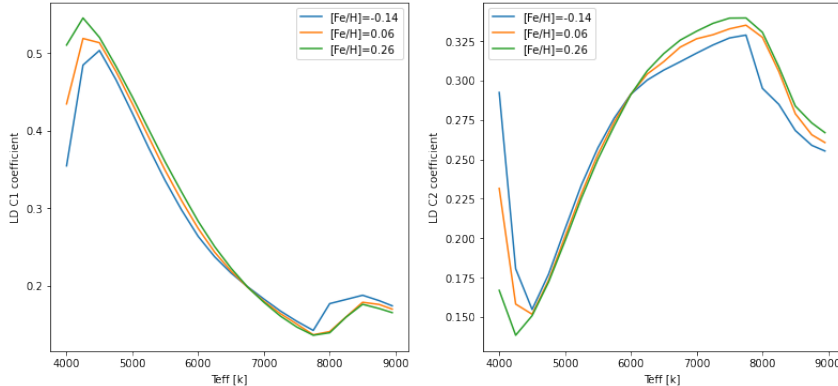


Fig. A.5: LD coefficients trend in the $T_{eff} - [Fe/H]$ plane

we treat data this way. In fact, changing secondary atmospheric parameters (g and $[Fe/H]$) now produces a still modest, but visible scatter. This is confirmed by the Montecarlo analysis, that yields results compatible with the previous case but with larger errorbars. The procedure could be repeated in the same way by fixing metallicity instead.

	c_1	σ_{c1}	c_2	σ_{c2}
Fixed $\log g$ Median:	0.3650	0.0276	0.2436	0.0156

Appendix A.2: Claret 2018

A followup paper (Claret 2018) provided a new method to model the LD coefficients dependency on atmospheric parameters. We'd like to check if this leads to different results with respect to Claret 2017. Unfolding the table requires the same procedure we've already described. Just note that in both cases we fix metallicity, and for the 2018 table metallicity must be fixed to 0, since the method is conceived for zero-metallicity stars.

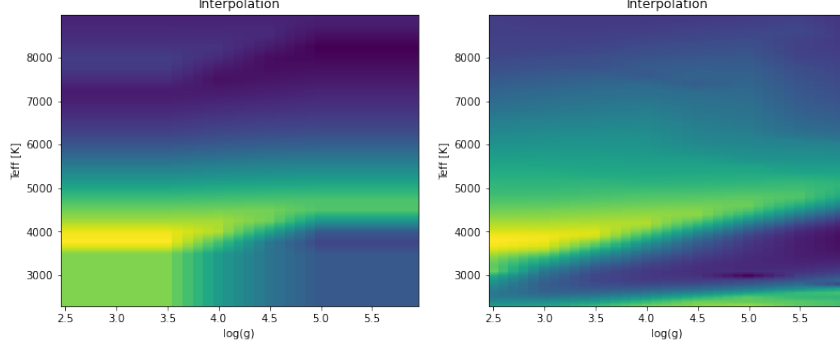


Fig. A.6: Comparison between interpolated matrices at fixed metallicity, to the stellar metallicity (2017 left), and to 0 (2018 right).

And finally we can display the dependency of the LD coefficients for the two-parameters game.

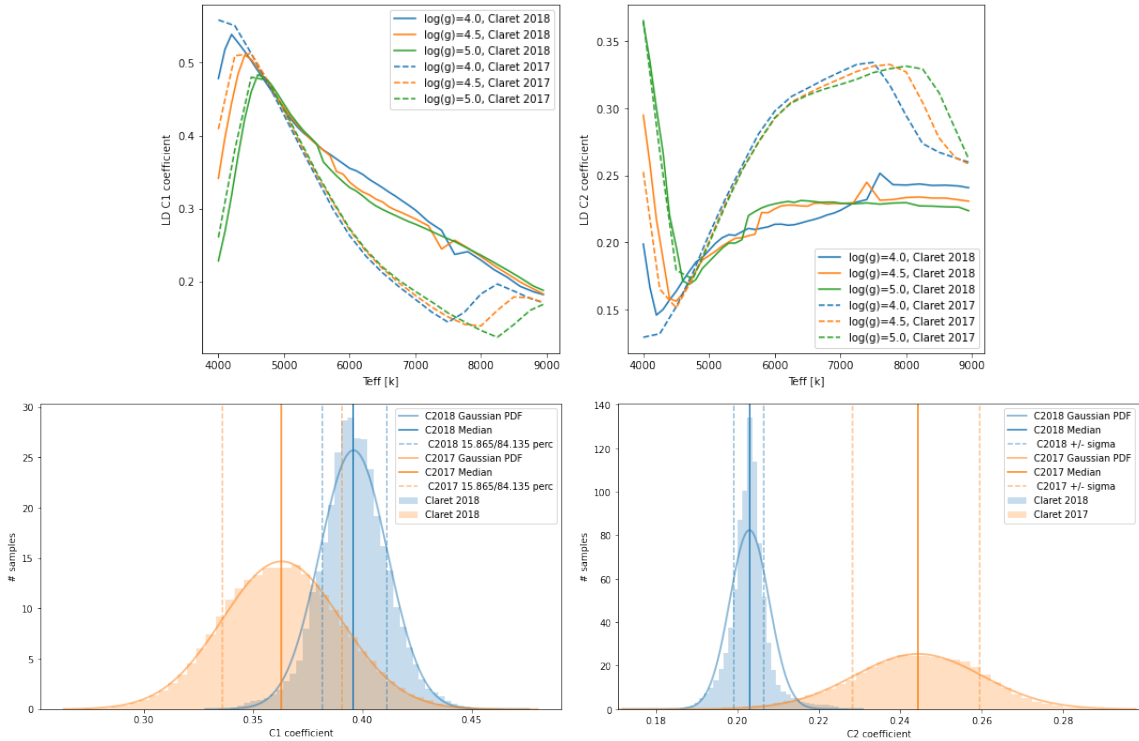


Fig. A.7: c_1 and c_2 trend, and comparison between the final results. Gaussian bells of the 2018 model are narrower.

First, the degeneracy on g and $[Fe/H]$ is completely removed, so that they can no longer be referred to as "secondary parameters". The comparison above shows that choosing the model will influence, even strongly, the estimate of the parameters. Quantitatively, the region characterised by $T \approx 5400K$ is one of the least affected by model choice, but the difference is still too wide to be neglected. The final estimates for the parameters are also quite different, both in terms of value and in terms of error. This indicates a systematic difference caused by the choice of the model. Because of this, we need to artificially inflate the error before using limb darkening parameters. This is very important especially for shallow transits like ours. Anyway, they're largely compatible still: see how each value is within a few errorbars away from the other. The model from Claret 2018 yields results with smaller errorbars for both coefficients.

	c_1	σ_{c1}	c_2	σ_{c2}
2017 Median	0.3631	0.0272	0.2444	0.0157
2018 Median	0.3961	0.0155	0.2030	0.0048

Appendix A.3: Claret 2011

We use another table from an older paper (Claret et al. 2011) by the same author, this time including filters. The header of our dataset shows that the filter r^* was used (SDSS). Remember that transits look differently when observed through different filters, and also that boxier transits make ingress/egress time determination easier. r^* filter was selected (SDSS), since it is the best choice in terms of CCD efficiency and in terms boxiness of the transit, making it easier to determine ingress and egress time, and therefore central time of transit. The unfolding technique of the data pack is always the same. This time, we account for stellar models (ATLAS/PHOENIX) and interpolation technique (least squares/flux conservation), for a grand total of 4 combinations. These are the very final results.

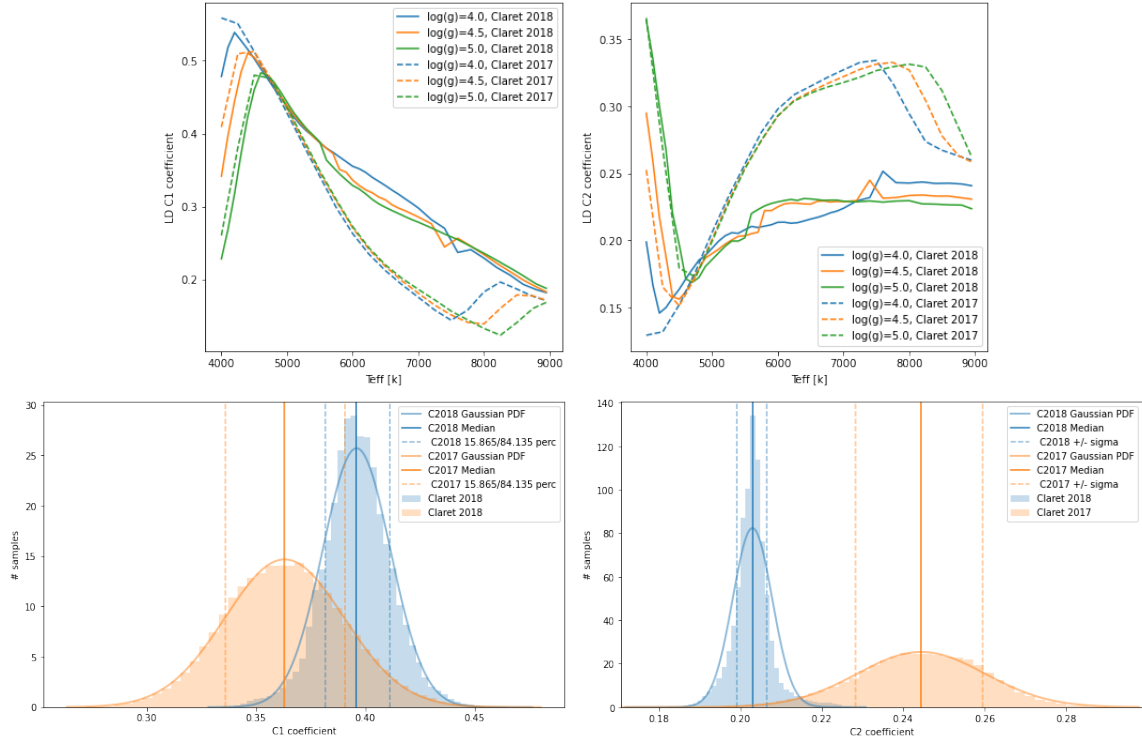


Fig. A.8: c_1 and c_2 trend, and comparison between the final results

Again, see how the choice of the model is deeply influencing the trend of the coefficients with respect to the atmospheric parameters, and the results consequently. Despite being compatible between each other, the estimates of the coefficients are quite

	c_1	σ_{c1}	c_2	σ_{c2}
ATLAS, LS:	0.4701	0.0367	0.2327	0.0231
ATLAS, FC:	0.4848	0.0347	0.2142	0.0205
PHOENIX, LS:	0.5251	0.0219	0.1728	0.0098
PHOENIX, FC:	0.5434	0.0212	0.1499	0.0088

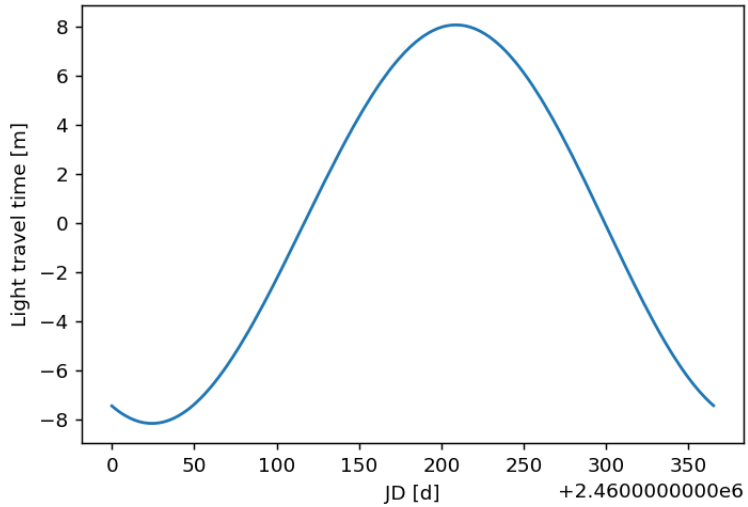
detached from the one inferred following Claret 2017 and Claret 2018. This reinforces the need to add a systematic error term.

Note that changing stellar model means changing the way we compute the gradient of temperature and the flux in stellar photosphere. In our case, Phoenix stellar model seems to be associated with slightly thinner errorbars, but the difference from ATLAS is not a relevant one.

Appendix B: Time correction

When reducing TASTE data and dealing with *sentinel.dat* output, we need to properly convert the time series, contained in columns two of the datatable. To do that, first we convert from minutes to days, then add the zero-point in Julian Date format, and finally also add half exposure time (after proper conversion in days).

Moreover, we can make use of the *Time* method to keep count of the time taken by the light to travel from the source position to the location of the observatory (Cima Ekar, Asiago). Since the Earth is in motion, light time travel is variable and follows a sinusoidal behaviour.



As a result, all times were converted from Julian Days expressed in the Universal Coordinated Time (JD_UTC), which is a geocentric reference frame, into Julian Days in the barycentric reference frame of the Solar System (BJD_TDB), which is given by the sum of the time at the Earth barycenter and the light travel time.

Appendix C: Figures

Appendix C.1: TESS and TASTE

Corner plots are generated as a result of PyORBIT and are plotted using the *corner* package. Along the diagonal there are histograms of the estimated 1D posterior probability distribution for each parameter. The histograms show that the recovered parameters are both accurate (close to injected value) and precise (narrow posterior distribution). The off-diagonal plots are the 2D histograms of the estimated joint posterior probability distribution of each pair of parameters, which show the correlation between pairs of parameters. The gray-scale map indicate the density of samples derived from MCMC simulation.

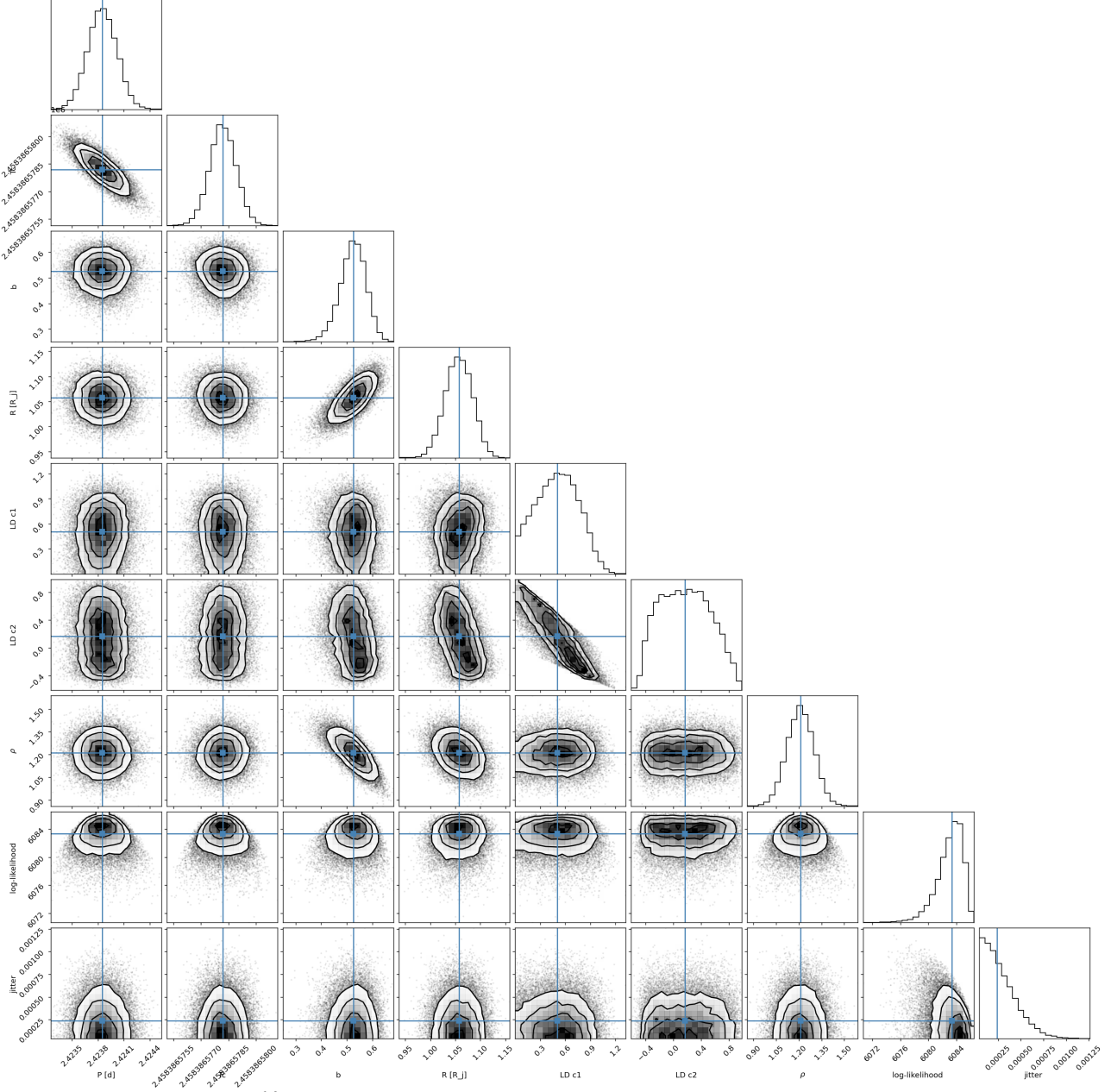


Fig. C.1: Correlation between TESS parameters. Each LD coefficient distribution is a little clumpy, and also there's evidence for severe correlation between the two. This suggests TESS estimation of LD coefficients is not fully trustworthy. More data could make corner plots more significant. Little anti-correlation is found between period and central time of transit, as well as little correlation between impact parameter and scaled radius.

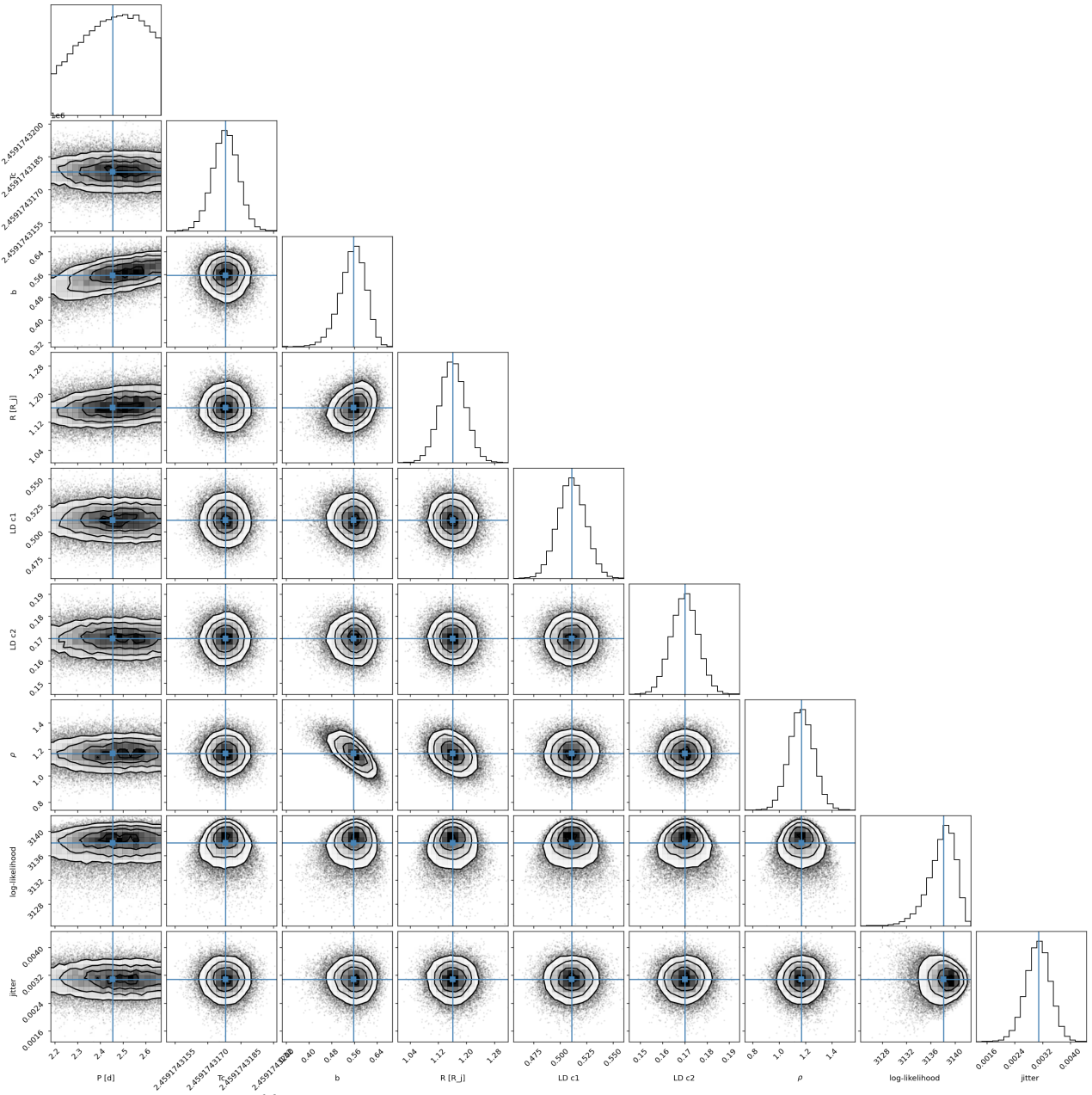


Fig. C.2: Correlation between TASTE parameters.

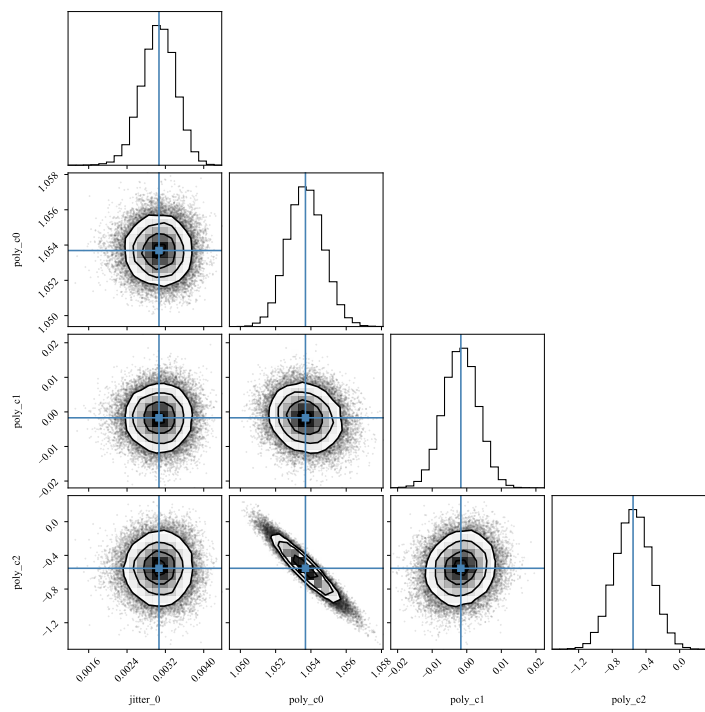


Fig. C.3: TASTE polynomial trend corner plot

Appendix C.2: Radial velocities

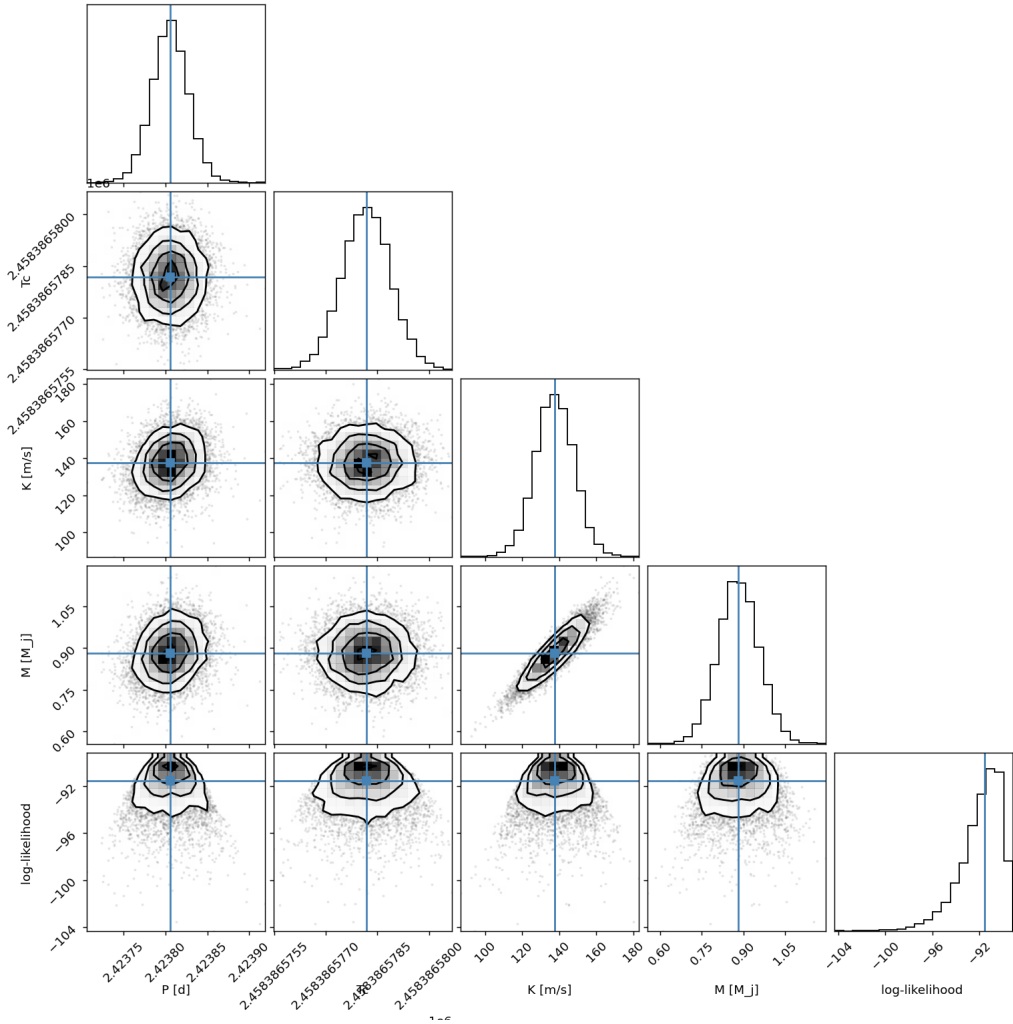


Fig. C.4: Correlation between parameters of the *radial velocities* model. Evidence of correlation is found for the mass versus velocity amplitude plot. The linear relation between the two implies some degree of degeneracy.

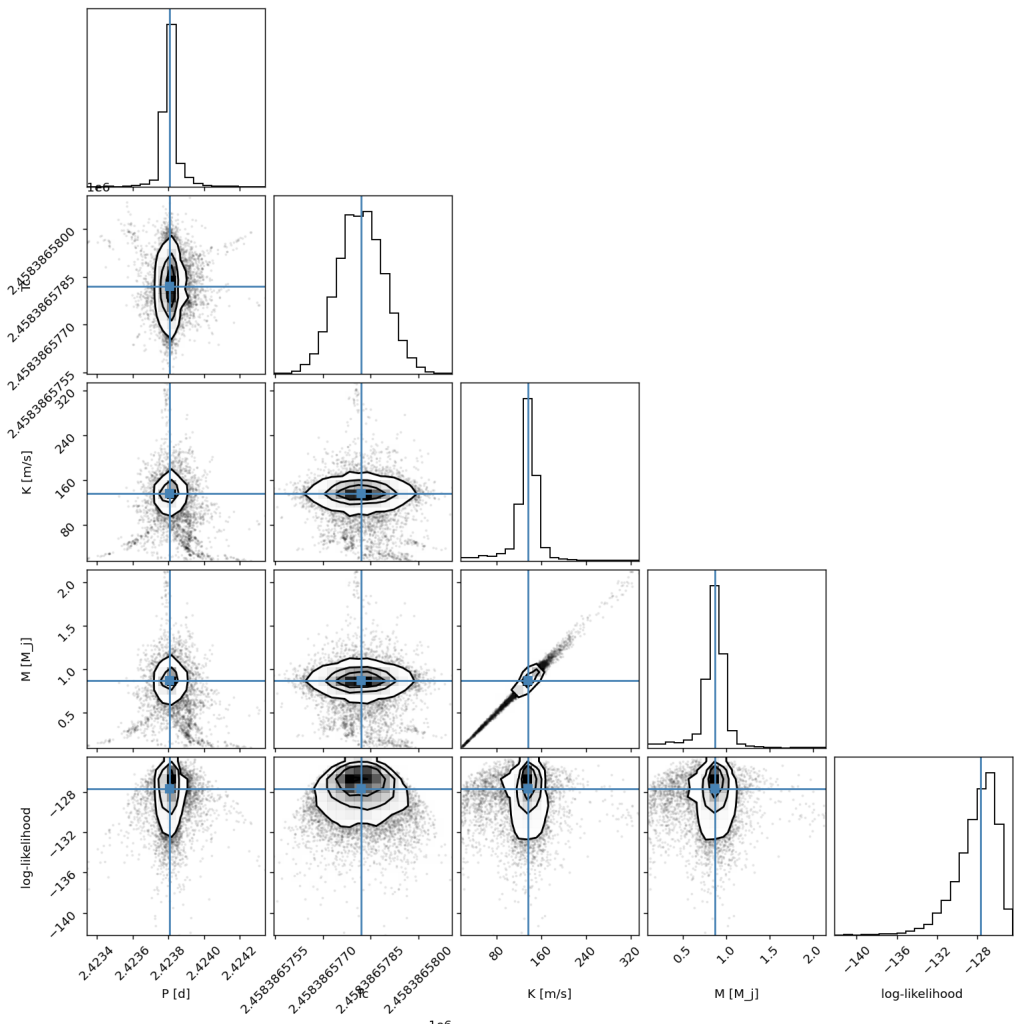


Fig. C.5: Correlation between parameters of the *harmonics* model